energies

MDPI

Article

Integral Sliding-Mode Control-Based Direct Power Control for Three-Level NPC Converters

Hao Lin [1], Jose I. Leon [1,2,*], Wensheng Luo [1], Abraham Marquez [2], Jianxing Liu [1], Sergio Vazquez [2] and L. G. Franquelo [1,2]

[1] Department of Control Science and Engineering, Harbin Institute of Technology, Harbin 150001, China; haolin@hit.edu.cn (H.L.); wensheng.luo@hit.edu.cn (W.L.); jx.liu@hit.edu.cn (J.L.); lgfranquelo@us.es (L.G.F.)

[2] Electronic Engineering Department, Universidad de Sevilla, 41004 Sevilla, Spain; amarquez@ieee.org (A.M.); sergi@us.es (S.V.)

* Correspondence: jileon@us.es

Received: 15 December 2019; Accepted: 30 December 2019; Published: 2 January 2020

Abstract: Three-level neutral-point-clamped (NPC) converter is widely used in energy conversion systems due to its good properties for high-power systems presenting output waveforms with reduced harmonic distortion. To obtain better system performance, an integral sliding-mode control (ISMC)-based direct power control (DPC) strategy is proposed for NPC converters. The controller achieves three objectives. First, an extended state observer (ESO)-based ISMC strategy, to enforce the active and reactive power to their reference values, is applied in the power tracking loop. ESO is used to reduce the influence of parameter uncertainties. Next, in the voltage regulation loop, a radial basis function neural network (RBFNN)-based adaptive ISMC strategy is applied to regulate the DC-link voltage. RBFNN is used to estimate the load variation, which is considered as a disturbance, to improve the system disturbance rejection ability. An adaptive law is used in the controller to reduce the chattering of reference active power which can reduce the current harmonic distortion. Finally, a proportional-integral (PI) control strategy is applied in the voltage balancing loop to achieve voltage balance between two DC-link capacitors. Experimental results show the effectiveness and superiority of the proposed control strategy for the NPC power converter compared with PI-based DPC strategy.

Keywords: three-level neutral-point-clamped converter; integral sliding-mode control; extended state observer; radial basis function neural network

1. Introduction

In recent years, grid-connected controlled rectifiers, also called active front end (AFE) have been widely used in motor drives [1], renewable energy sources [2,3], DC microgrids [4], etc. AFE can not only improve the power factor, but also is robust against the fluctuations of the grid, with excellent dynamic characteristics [5]. Multilevel converters have been widely used as AFEs in industrial applications for their high rated power and high quality output waveforms [6,7], such as neutral-point-clamped (NPC) and cascaded H-bridge [8]. Three-level NPC is generally recognized as one of the most popular topologies among different multilevel converters. The circuit topology of the NPC is relatively simple compared with other converters, and in high-power systems, NPC has a good trade-off between cost and performance [9].

The control strategies for the NPC converter can be divided into two categories, the current based controllers and direct power control (DPC) [10]. Based on the instantaneous reactive power defined in [11], DPC is a well-known efficient control strategy for power systems, and this strategy enforces the active power and reactive power to the reference values by choosing the best state of the power

semiconductors through a look up table. In industrial applications, DPC shows its good dynamic performance, but owns a variable switching frequency. To overcome this drawback, a DPC using space vector modulation is proposed in [12]. In [13], the constant switching frequency is achieved by combining DPC with a predictive selection of a voltage vectors sequence. In this paper, for the power tracking loop, DPC based on level shifted-pulse width modulation (LS-PWM) strategy is employed to track active power and reactive power to their reference values with constant switching frequency.

On the other hand, proportional-integral (PI) control strategy has become an attractive method due to its easy implementation, low cost and satisfactory performance [14]. The control structure of PI-based DPC for the NPC converter is shown in Figure 1, and the controller design is included in Appendix A. The PI control strategy is applied in power tracking loop, voltage regulation loop and voltage balancing loop. However, PI control strategy can not perform well with load variations [15]. To overcome this problem, in this paper, an integral sliding-mode control (ISMC) strategy is used in DPC for the power tracking loop and the voltage regulation loop. ISMC has been the focus of research in recent years. In [16], an ISMC and a fixed control allocation technique are used to estimate the matched faults. Ref. [17] proposes a fuzzy ISMC for permanent magnet synchronous generator-based wind energy conversion systems. The performance, problems and some improvements of ISMC are shown in [18]. ISMC not only maintains the advantages of traditional sliding-mode control (SMC) such as insensitivity and robustness to the disturbances, but also has a more accurate and quicker tracking performance. In the ISMC strategy, the system states are on the sliding-mode surface from the beginning which eliminates the reaching phase of the sliding-mode variable, and the convergence time of the tracking error is reduced [19]. The chattering of the controller is a challenge of traditional SMC [20]. The traditional ways of reducing chattering are introduced in [21]. In [22], evolutionary algorithms are used to tune the constrained parameters of the controller, which reduces the convergence time of tracking error and the chattering. In this paper, a simple adaptive law is applied in the voltage tracking loop to reduce the chattering of reference active power which can reduce the current harmonic distortion.

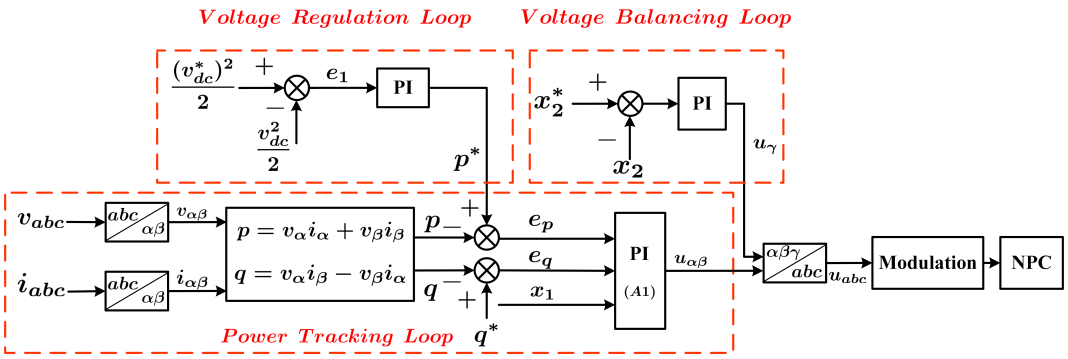

Figure 1. Control structure of PI-based DPC.

In addition, parameter uncertainties of grid frequency and inductor, disturbances such as the load variation will affect the system performance. Hence, observer-based control strategy has been taken into account to improve the robustness and disturbance rejection ability of the controller [23,24]. Extended state observer (ESO) is a widely used estimation approach, which can be used to estimate both disturbances and system states. It is proved that the higher order ESO can improve the tracking ability of fast-varying sinusoidal disturbances in [25]. In [26], several disturbance observers, such as ESO, unknown input observer, uncertainty and disturbance estimator, are analyzed and compared. In [27], ESO is used to estimate the total uncertainties of a class of nonlinear dynamical systems with zero dynamics. In ESO, the disturbances such as unmodeled dynamics, parameter uncertainties and load variations are treated as a new system state. Then based on the Hurwitz theory, the parameters can be chosen to guarantee the estimation error converging to zero. In this paper, an ESO is used in the power tracking loop to estimate the parameter uncertainties of grid frequency and inductor,

with only one parameter to be adjusted. However, as the dynamics of estimation error is exponential with negative exponent, the error can only converge to zero in infinite time. Considering that the load variation will influence the reference of active power and that results in current total harmonic distortion (THD) increasing, the effect of load variation on system performance is much bigger than that of the uncertainties. In this paper, a radial basis function neural network (RBFNN) observer is used in the voltage regulation loop to estimate the load variation. RBFNN is another widely used effective observer. The structure and stability analysis of RBFNN are introduced in [28]. RBFNN is used in [29] to help to solve the problem of detecting and locating circular holes in conducting plates. In [30], RBFNN is applied for NPC to estimate the unknown functions including parameter uncertainties in the power tracking loop, and the stability is approved. In [31], to approximate the equations of stochastic nonlinear systems, RBFNN is used to estimate the state variables. Based on the stability proof of the voltage regulation loop, the estimation error can converge to zero in finite time, but the number of parameters needed to tune are large. Therefore, the use of ESO in the power tracking loop and RBFNN in the voltage regulation loop can not only guarantee the system performance, but also reduce the number of system parameters as much as possible to reduce the controller design complexity.

The rest paper is organized as follows. In Section 2, the topology and mathematical model of three-phase three-level NPC converter, the control objectives and the fundamental knowledge of RBFNN are demonstrated. The control strategies of power tracking loop, voltage regulation loop and voltage balancing loop are designed in Section 3. The parameter tuning of the proposed strategy is shown in Section 4. The experimental results compared with traditional PI-based DPC strategy are shown and analyzed in Section 5. Finally, a brief conclusion is given in Section 6.

2. System Description and Preliminaries

2.1. System Description and Modeling

The circuit diagram of the three-phase three-level NPC converter is introduced in Figure 2. The converter is grid-tied through the inductors L at the AC side. The converter consists of three legs, each leg has four IGBTs and two diodes, and the midpoints of each leg are connected. The system variables are described in Table 1. The mathematical model of the NPC converter [10] can be depicted as follows:

$$\begin{aligned} L\frac{di_a}{dt} &= v_a - \frac{x_1}{6}(2u_a - u_b - u_c) - \frac{x_2}{6}(2u_a^2 - u_b^2 - u_c^2), \\ L\frac{di_b}{dt} &= v_b - \frac{x_1}{6}(-u_a + 2u_b - u_c) - \frac{x_2}{6}(-u_a^2 + 2u_b^2 - u_c^2), \\ L\frac{di_c}{dt} &= v_c - \frac{x_1}{6}(-u_a - u_b + 2u_c) - \frac{x_2}{6}(-u_a^2 - u_b^2 + 2u_c^2), \end{aligned} \tag{1}$$

$$C\dot{x}_1 = u_{abc}^T i_{abc} - 2i_{dc}, \tag{2}$$

$$C\dot{x}_2 = \left(u_{abc}^2\right)^T i_{abc}, \tag{3}$$

where $x_1 = V_{dc1} + V_{dc2}$ is the sum of two DC-link capacitor voltages, and $x_2 = V_{dc1} - V_{dc2}$ is the difference of the two DC-link capacitor voltages.

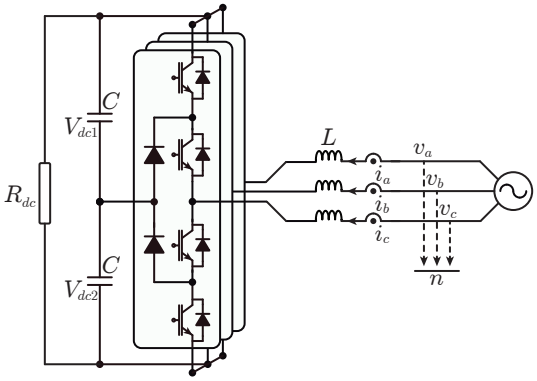

Figure 2. The three-phase three-level NPC converter topology.

Table 1. System variables.

Variable	Description
$i_{abc} = \{i_a, i_b, i_c\}^T$	Inductor currents in *abc* reference frame
$v_{abc} = \{v_a, v_b, v_c\}^T$	Grid voltages in *abc* reference frame
$u_{abc} = \{u_a, u_b, u_c\}^T$	Average duty cycles in *abc* reference frame
$i_{\alpha\beta} = \{i_\alpha, i_\beta\}^T$	Inductor currents in $\alpha\beta$ reference frame
$v_{\alpha\beta} = \{v_\alpha, v_\beta\}^T$	Grid voltages in $\alpha\beta$ reference frame
$u_{\alpha\beta\gamma} = \{u_\alpha, u_\beta, u_\gamma\}^T$	Average duty cycles in $\alpha\beta\gamma$ reference frame
L, C	Phase inductor and DC-link capacitor
R_{dc}	Load resistance
V_{dc1}, V_{dc2}	DC-link capacitor voltages
ω	Grid frequency

In order to facilitate the controller design, transforming the above Equations (1)–(3) with the Clark transformation matrix, the system dynamics in the $\alpha\beta$ reference frame (4)–(6) can be obtained [10].

$$\begin{aligned} L\frac{di_\alpha}{dt} &= v_\alpha - \frac{1}{2}x_1 u_\alpha + x_2\left(\frac{1}{2\sqrt{6}}\left(u_\beta^2 - u_\alpha^2\right) - \frac{1}{\sqrt{3}}u_\alpha u_\gamma\right), \\ L\frac{di_\beta}{dt} &= v_\beta - \frac{1}{2}x_1 u_\beta + x_2\left(\frac{1}{\sqrt{6}}\left(u_\alpha u_\beta\right) - \frac{1}{\sqrt{3}}u_\beta u_\gamma\right), \end{aligned} \tag{4}$$

$$C\dot{x}_1 = u_{\alpha\beta}^T i_{\alpha\beta} - 2\frac{x_1}{R_{dc}}, \tag{5}$$

$$C\dot{x}_2 = \frac{2}{\sqrt{6}}\left(\left(u_\alpha^2 - u_\beta^2\right) i_\alpha - u_\alpha u_\beta i_\beta\right) + \frac{1}{\sqrt{6}}u_{\alpha\beta}^T i_{\alpha\beta} u_\gamma. \tag{6}$$

It can be calculated that the third terms in the right hand of the two equations in (4) have lower order of magnitude than the first and second terms [10], then (4) can be simplified into

$$\begin{aligned} L\frac{di_\alpha}{dt} &= v_\alpha - \frac{1}{2}x_1 u_\alpha, \\ L\frac{di_\beta}{dt} &= v_\beta - \frac{1}{2}x_1 u_\beta. \end{aligned} \tag{7}$$

According to the definition of active power and instantaneous reactive power in [11], the active power, reactive power and their derivatives can be obtained.

$$\begin{aligned} p &= v_{\alpha\beta}^T i_{\alpha\beta}, \\ q &= v_{\alpha\beta}^T J i_{\alpha\beta}, \end{aligned} \tag{8}$$

$$\begin{aligned} L\dot{p} &= ||v_{\alpha\beta}||^2 - \frac{1}{2}x_1 v_{\alpha\beta}^T u_{\alpha\beta} + L\omega q, \\ L\dot{q} &= -\frac{1}{2}x_1 (Jv_{\alpha\beta})^T u_{\alpha\beta} - L\omega p, \end{aligned} \tag{9}$$

where $J = \begin{bmatrix} 0 & -1 \\ 1 & 0 \end{bmatrix}$.

2.2. Control Objectives

The general control objectives of the three-phase three-level NPC converter can be stated as follows:

1. The instantaneous reactive power q and active power p should be enforced to their reference values q^* and p^*, respectively.

$$\begin{aligned} p &\to p^*, \\ q &\to q^*. \end{aligned} \tag{10}$$

2. The sum voltage of the two DC-link capacitors x_1 should track its reference value x_1^* defined by the operator.

$$x_1 \to x_1^*. \tag{11}$$

3. The voltages of the two DC-link capacitors should be balanced which means the voltage difference x_2 should be regulated to zero.

$$x_2 \to x_2^* = 0. \tag{12}$$

2.3. RBFNN Preliminaries

In this paper, to improve the disturbance rejection ability, a RBFNN is applied to estimate the nonlinear function $\gamma(t)$ in the voltage regulation loop. RBFNN is a feed-forward neural network made up of input layer, hidden layer and output layer. It can accurately estimate any smooth nonlinear functions, and it has good local approximation performance. Based on RBFNN in [30], the function $\gamma(t)$ can be depicted as

$$\gamma(t) = \theta^* \xi(t) + \varepsilon = \begin{bmatrix} \theta^* & \varepsilon \end{bmatrix} \begin{bmatrix} \xi \\ 1 \end{bmatrix} = \Theta^T \varsigma, \tag{13}$$

where θ^* is a unknown ideal weight parameter vector. ε is the approximation error. $\xi(t) = [\xi_1(t), \xi_2(t), \ldots, \xi_n(t)]^T$ is a known basis function vector with the neural network node number $n > 1$, and it's usually chosen as Gaussian function with the form

$$\xi_i(t) = \exp^{(-\frac{(t-c_i)^2}{\delta^2})}, \quad i = 1, 2 \ldots, n, \tag{14}$$

where c_i denotes the center of $\xi_i(t)$, and δ denotes the width of $\xi_i(t)$.

3. Controller Design

To achieve the three objectives, in this paper, the controller consists of three parts, including a power tracking loop, a voltage regulation loop, and a voltage balancing loop. An ESO-based ISMC strategy is applied in the power tracking loop to ensure the fast convergence of the active power and reactive power to their reference values. The reference value of active power is the output of voltage regulation loop, and the reference value of reactive power is set to zero to achieve unity power factor. In the voltage regulation loop, a RBFNN-based ISMC is applied to enforce the DC-link voltage to its reference value. Considering the relationship between inductor currents and active and reactive power in (8), the control of inductor currents can be achieved by the control of active and reactive power. In the voltage balancing loop, a PI control strategy is used to balance the voltages of two DC-link capacitors. The control structure is shown in Figure 3. In what follows, the design of the controller is stated.

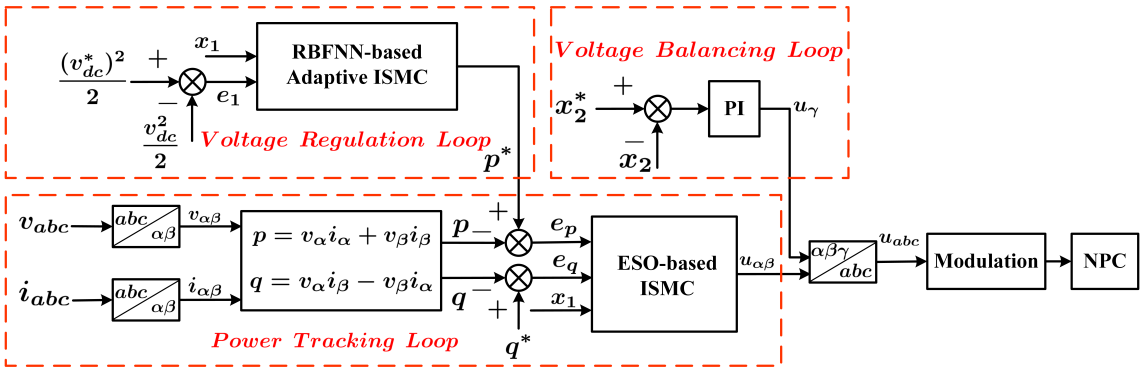

Figure 3. The control structure of the proposed strategy.

3.1. Power Tracking Loop

In this section, an ESO-based ISMC strategy is applied to enforce the active power and reactive power to the reference values. The control structure of power tracking loop is shown in Figure 4. The controller is based on the zero equilibrium controller $u_{\alpha\beta}^{eq}$. The disturbances d_p and d_q including parameter uncertainties are estimated by an ESO, and the estimations are applied in the controller to improve the robustness. First, define the tracking error of p and q as

$$\begin{aligned} e_p &= p^* - p, \\ e_q &= q^* - q. \end{aligned} \tag{15}$$

Then, the derivative of (15) can be obtained with (9).

$$\begin{aligned} \dot{e}_p &= \dot{p}^* - \frac{||v_{\alpha\beta}||^2}{L} + \frac{1}{2L} x_1 v_{\alpha\beta}^T u_{\alpha\beta} - \omega q, \\ \dot{e}_q &= \dot{q}^* + \frac{1}{2L} x_1 (J v_{\alpha\beta})^T u_{\alpha\beta} + \omega p. \end{aligned} \tag{16}$$

Considering the parameter uncertainties, the actual values of L and ω can be described as

$$L_r = L + \Delta L, \quad \omega_r = \omega + \Delta\omega, \tag{17}$$

where ΔL and $\Delta\omega$ are considered as the parametric uncertainties. Substituting (17) into (16), it can be obtained that

$$\begin{aligned}
\dot{e}_p &= \dot{p}^* - \frac{||v_{\alpha\beta}||^2}{L+\Delta L} + \frac{1}{2(L+\Delta L)} x_1 v_{\alpha\beta}^T u_{\alpha\beta} - (\omega+\Delta\omega)q \\
&= -\frac{||v_{\alpha\beta}||^2}{L} + \frac{1}{2L} x_1 v_{\alpha\beta}^T u_{\alpha\beta} - \omega q + d_p, \\
\dot{e}_q &= \dot{q}^* + \frac{1}{2(L+\Delta L)} x_1 (Jv_{\alpha\beta})^T u_{\alpha\beta} + (\omega+\Delta\omega)p \\
&= \frac{1}{2L} x_1 (Jv_{\alpha\beta})^T u_{\alpha\beta} + \omega p + d_q.
\end{aligned} \tag{18}$$

where

$$\begin{aligned}
d_p &= \dot{p}^* - (\frac{1}{L_r} - \frac{1}{L})||v_{\alpha\beta}||^2 + (\frac{1}{2L_r} - \frac{1}{2L}) x_1 v_{\alpha\beta}^T u_{\alpha\beta} - (\omega_r - \omega)q, \\
d_q &= \dot{q}^* + (\frac{1}{2L_r} - \frac{1}{2L}) x_1 (Jv_{\alpha\beta})^T u_{\alpha\beta} + (\omega_r - \omega)p.
\end{aligned} \tag{19}$$

When the tracking errors of active power and reactive power converge to zero, the derivatives of p and q are equal to zero, and the controller $u_{\alpha\beta}$ is equal to zero equilibrium controller $u_{\alpha\beta}^{eq} = \begin{bmatrix} u_\alpha^{eq} & u_\beta^{eq} \end{bmatrix}^T$. Define $\dot{p} = 0$ and $\dot{q} = 0$, then (20) can be obtained. The zero equilibrium controller (21) can be obtained by solving (20). Then the controller $u_{\alpha\beta}$ of the power tracking loop can be designed as (22).

$$\begin{aligned}
v_\alpha u_\alpha^{eq} + v_\beta u_\beta^{eq} &= \frac{2\left(||v_{\alpha\beta}||^2 + L\omega q\right)}{x_1}, \\
v_\alpha u_\beta^{eq} - v_\beta u_\alpha^{eq} &= -\frac{2L\omega p}{x_1},
\end{aligned} \tag{20}$$

$$u_{\alpha\beta}^{eq} = \frac{2}{x_1||v_{\alpha\beta}||^2}\left[\left(||v_{\alpha\beta}||^2 + L\omega q\right) v_{\alpha\beta} - L\omega p J v_{\alpha\beta}\right], \tag{21}$$

$$u_{\alpha\beta} = u_{\alpha\beta}^{eq} - \mu(e_p) v_{\alpha\beta} - \mu(e_q) J v_{\alpha\beta}, \tag{22}$$

where $\mu(e_p)$ and $\mu(e_q)$ are the integral sliding-mode controllers to be designed. Substituting (22) into (18), the dynamics of power tracking errors can be derived as

$$\dot{e} = B\mu + d, \tag{23}$$

where $e = \begin{bmatrix} e_p & e_q \end{bmatrix}^T$, $B = -\frac{x_1}{2L}||v_{\alpha\beta}||^2$, $\mu = \begin{bmatrix} \mu(e_p) & \mu(e_q) \end{bmatrix}^T$, $d = \begin{bmatrix} d_p & d_q \end{bmatrix}^T$. An ESO is applied to estimate d_p and d_q with the following structure [32],

$$\begin{aligned}
\dot{\hat{e}}_j &= -\frac{x_1}{2L}||v_{\alpha\beta}||^2 \mu(e_j) + \hat{d}_j + 2\omega_j(e_j - \hat{e}_j), \\
\dot{\hat{d}}_j &= \omega_j^2 (e_j - \hat{e}_j),
\end{aligned} \tag{24}$$

where $j \in \{p, q\}$, and $\omega_j > 0$ to make sure that $s^2 + 2\omega_j s + {\omega_j}^2$ is Hurwitz. The damping ratio of the observer is 1, and the bandwidth is determined by ω_j, which is $\omega_b = \omega_j\sqrt{\sqrt{2}-1}$. Generally speaking, the bandwidth will influence not only the observation rate and accuracy, but also the noise sensitivity. If the variation rate of d_j is fast, the bandwidth needs to be high enough to obtain an exact estimation, but the noise sensitivity will increase and the disturbance rejection ability will decrease. As a result, the estimation performance and noise tolerance should be considered when choosing ω_j.

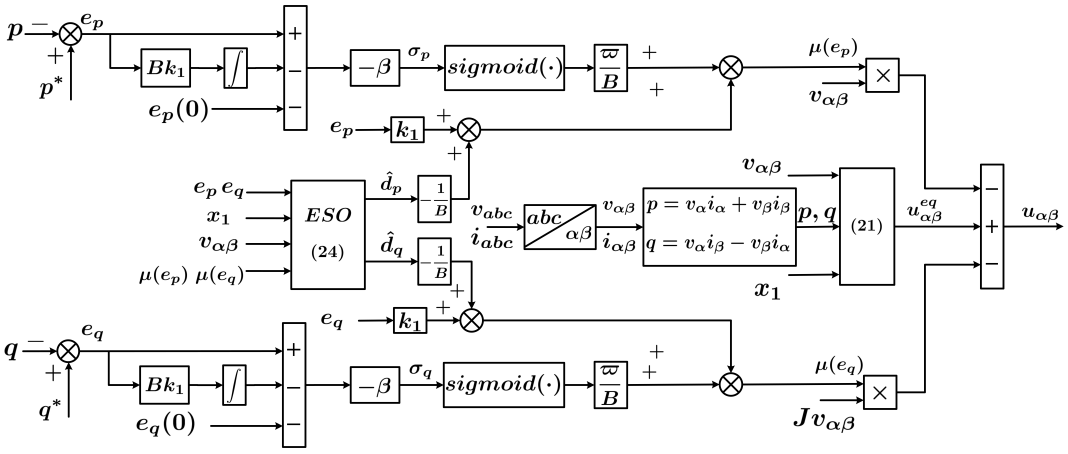

Figure 4. Control structure of power tracking loop.

The system is stable when the sliding-mode variable and control law are defined as

$$\begin{aligned}\sigma &= \begin{bmatrix} \sigma_p & \sigma_q \end{bmatrix}^T \\ &= -\beta\left(e(t) - e(0) - \int_0^t \left(B\mu_1(s) + \hat{d}(s)\right) ds\right), \end{aligned} \tag{25}$$

$$\mu = \mu_1 + \frac{1}{B}\mu_N, \tag{26}$$

$$\mu_1 = k_1 e - \frac{1}{B}\hat{d}, \tag{27}$$

$$\mu_N = \varpi\begin{bmatrix} sigmoid(\sigma_p) & sigmoid(\sigma_q) \end{bmatrix}^T, \tag{28}$$

where $\varpi \geq \tilde{d}_M$, $\tilde{d}_M = \sup_{t>0}(||\tilde{d}||)$, $\tilde{d} = \begin{bmatrix} \tilde{d}_p & \tilde{d}_q \end{bmatrix}^T = \begin{bmatrix} d_p - \hat{d}_p & d_q - \hat{d}_q \end{bmatrix}^T$, and $sigmoid(\sigma_j) = 2/(1 + \exp^{(-10^5 * \sigma_j)}) - 1$. This sigmoid function is employed to replace the *sign* function, which can help reducing the chattering of μ.

Next, the stability of the ESO-based ISMC of the power tracking loop is proved. Construct the Lyapunov function as $V = \frac{1}{2}\sigma^2$. The derivatives of σ and V can be derived as (29) and (30).

$$\begin{aligned}\dot{\sigma} &= -\beta\left(B\mu + d - B\mu_1 - \hat{d}\right) \\ &= -\beta\mu_N - \beta\tilde{d}, \end{aligned} \tag{29}$$

$$\begin{aligned}\dot{V} &= \sigma^T\dot{\sigma} \\ &= -\beta\sigma^T\mu_N - \beta\sigma^T\tilde{d} \\ &= -\beta\left(\varpi\sigma_p sigmoid(\sigma_p) + \varpi\sigma_q sigmoid(\sigma_q)\right) - \beta(\sigma_p\tilde{d}_p + \sigma_q\tilde{d}_q). \end{aligned} \tag{30}$$

Based on the equation of sigmoid function, the function value will be greater than -1 and less than 1 only when the sliding-mode variable σ_j is between -10^{-4} to 10^{-4}, and when the sliding-mode variables reach this order of magnitude, it can be counted that the system states have arrived the sliding-mode surface. This implies that $\dot{V} < 0$ before the system states arrive the sliding-mode surface. With this conclusion, the reachability condition of sliding-mode can be reached.

Next, the stability of the proposed controller is analyzed. The equivalent control law $\mu_N^{eq} = -\tilde{d}$ can be obtained by solving $\dot{\sigma} = 0$. Substituting $\mu^{eq} = \mu_1 + \frac{1}{B}\mu_N^{eq}$ into (23), the derivatives of power tracking errors can be described as follows:

$$\begin{aligned} \dot{e} &= B\mu^{eq} + d \\ &= B\mu_1 + \mu_N^{eq} + d \\ &= Bk_1 e - \hat{d} + \mu_N^{eq} + d \\ &= -\frac{x_1}{2L}||v_{\alpha\beta}||^2 k_1 e. \end{aligned} \tag{31}$$

It can be obtained that the tracking errors converge to zero when $t \to \infty$, and the power tracking loop is asymptotically stable.

3.2. Voltage Regulation Loop

In this section, a RBFNN-based adaptive ISMC control strategy is applied to regulate the DC-link voltage to its reference value. The control strategy of voltage regulation loop is introduced in Figure 5. Assuming that the power tracking loop acts faster than the voltage regulation loop, the tracking errors of p and q can be considered as zero and $p = p^*$. Then the voltage equation (5) can be rewritten as

$$Cx_1\dot{x}_1 = 2p^* - \frac{2x_1^2}{R_{dc}}, \tag{32}$$

where $p^* = \frac{1}{2}x_1 u_{\alpha\beta}^T i_{\alpha\beta}$ is output of voltage regulation loop and the input of power tracking loop as the reference value of active power. Then (32) can be rewritten as

$$\dot{z}_1 = \frac{2}{C}u_v - p_{load}, \tag{33}$$

where $z_1 = \frac{1}{2}x_1^2$, $u_v = p^*$, $p_{load} = \frac{2x_1^2}{C}\gamma$, and $\gamma = \frac{1}{R_{dc}}$. γ is considered as the unknown variable which is estimated by the above mentioned RBFNN approach. The observer is designed as follows:

$$\hat{\gamma} = \begin{bmatrix} \hat{\theta} & \hat{\varepsilon} \end{bmatrix} \begin{bmatrix} \xi \\ 1 \end{bmatrix} = \hat{\Theta}^T \varsigma, \tag{34}$$

$$\dot{\hat{\Theta}} = -x_1^2 \sigma_v \varsigma. \tag{35}$$

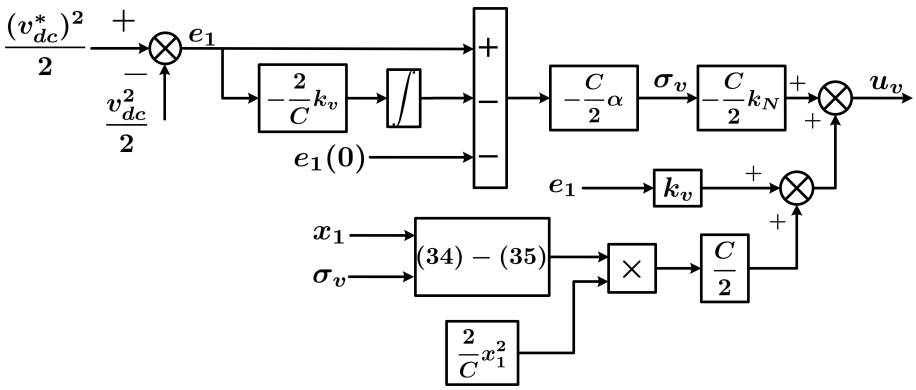

Figure 5. Control structure of voltage regulation loop.

Then the estimation of p_{load} is $\hat{p}_{load} = \frac{2x_1^2}{C}\hat{\gamma}$. Define the regulation error $e_1 = z_1^* - z_1$, and $z_1^* = \frac{1}{2}(x_1^*)^2$. The derivative of regulation error is

$$\dot{e}_1 = -\frac{2}{C}u_v + p_{load}. \tag{36}$$

The system is stable when the sliding-mode variable and control law are defined as (37)–(41). The sign function will increase the chattering of u_v, which will result in the THD of inductor currents increasing, the adaptive coefficient k_{Nv} is used to reduce this impact on the system performance.

$$\sigma_v = -\frac{C}{2}\alpha\left(e_1(t) - e_1(0) - \int_0^t\left(-\frac{2}{C}u_{1v}(s) + \hat{p}_{load}(s)\right)ds\right), \tag{37}$$

$$u_v = u_{1v} - \frac{C}{2}u_{Nv}, \tag{38}$$

$$u_{1v} = k_v e_1 + \frac{C}{2}\hat{p}_{load}, \tag{39}$$

$$u_{Nv} = k_{Nv}\text{sign}(\sigma_v), \tag{40}$$

$$k_{Nv} = k_N|\sigma_v|. \tag{41}$$

Next, the stability of the RBFNN-based ISMC for voltage regulation loop is proved. Define $\tilde{\Theta} = \Theta - \hat{\Theta}$, and construct the Lyapunov function $V_v = \frac{1}{2}\sigma_v^2 + \frac{1}{2}\alpha\tilde{\Theta}^T\tilde{\Theta}$. The derivatives of σ_v and V_v can be obtained.

$$\begin{aligned}
\dot{\sigma}_v &= -\frac{C}{2}\alpha\left(\dot{e}_1 + \frac{2}{C}u_{1v} - \hat{p}_{load}\right)\\
&= -\frac{C}{2}\alpha\left(-\frac{2}{C}u_v + p_{load} + \frac{2}{C}u_{1v} - \hat{p}_{load}\right)\\
&= \frac{C}{2}\alpha\left(-u_{Nv} - \tilde{p}_{load}\right)\\
&= \frac{C}{2}\alpha\left(-k_{Nv}\text{sign}(\sigma_v) - \tilde{p}_{load}\right)\\
&= -k_{Nv}\alpha\frac{C}{2}\text{sign}(\sigma_v) - \alpha x_1^2\tilde{\gamma},
\end{aligned} \tag{42}$$

$$\begin{aligned}
\dot{V}_v &= \sigma_v\dot{\sigma}_v + \alpha\tilde{\Theta}^T\dot{\tilde{\Theta}}\\
&= -k_{Nv}\alpha\frac{C}{2}|\sigma_v| - \alpha x_1^2\sigma_v\tilde{\gamma} - \alpha\tilde{\Theta}^T\dot{\hat{\Theta}}\\
&= -k_{Nv}\alpha\frac{C}{2}|\sigma_v| - \alpha x_1^2\sigma_v\tilde{\Theta}^T\varsigma - \alpha\tilde{\Theta}^T\dot{\hat{\Theta}}\\
&= -k_{Nv}\alpha\frac{C}{2}|\sigma_v|\\
&= -k_N\alpha\frac{C}{2}|\sigma_v|^2\\
&< 0,
\end{aligned} \tag{43}$$

where $\tilde{p}_{load} = p_{load} - \hat{p}_{load}$ and $\tilde{\gamma} = \tilde{\Theta}^T\varsigma$. It can be seen that the derivative of the Lyapunov function is less than zero, which means the states of the system will reach the sliding-mode surface $\sigma_v = 0$ in finite time, and the estimation error will converge to zero in finite time. The reachability is guaranteed.

Next, the stability of the controller is analyzed. The equivalent control law $u_{Nv}^{eq} = -\tilde{p}_{load}$ can be obtained by solving $\dot{\sigma}_v = 0$. Substituting $u_v^{eq} = u_{1v} - \frac{C}{2}u_{Nv}^{eq}$ into (36), the derivative of voltage regulation error can be obtained.

$$\begin{aligned}\dot{e}_1 &= -\frac{2}{C}u_v^{eq} + p_{load} \\ &= -\frac{2}{C}u_{1v} + u_{Nv}^{eq} + p_{load} \\ &= -\frac{2}{C}u_{1v} - \tilde{p}_{load} + p_{load} \\ &= -\frac{2}{C}u_{1v} + \hat{p}_{load} \\ &= -k_v\frac{2}{C}e_1. \end{aligned} \tag{44}$$

It can be seen that the regulation error converges to zero when $t \to \infty$, and the voltage regulation loop is asymptotically stable.

3.3. Voltage Balancing Loop

In this section, PI control strategy is applied to balance the voltages of two DC-link capacitors. The control structure of voltage balancing loop is introduced in Figure 6. Assuming that the power tracking loop acts faster than the voltage balancing loop, the tracking errors of p and q can be considered as zero. The derivative of unbalanced voltage error x_2 in (6) can be derived as

$$C\dot{x}_2 = \frac{2p^*}{\sqrt{6}x_1}u_\gamma + \phi, \tag{45}$$

where $\phi = \frac{2}{\sqrt{6}}\left((u_\alpha)^2 - (u_\beta)^2\right)i_\alpha - u_\alpha u_\beta i_\beta$. The control law is designed as

$$u_\gamma = -k_{pb}x_2 - k_{ib}\int_0^t x_2 ds, \tag{46}$$

where the parameters k_{pb} and k_{ib} are positive constants.

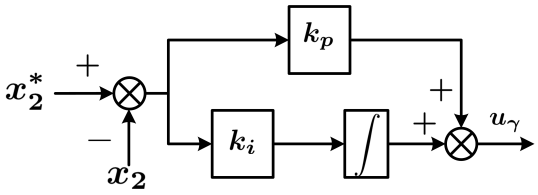

Figure 6. Control structure of voltage balancing loop.

4. Parameters Tuning of ISMC-Based DPC

For the power tracking loop and voltage regulation loop, the sliding-mode variables σ and σ_v are zero from the beginning if the exact initial values $e(0)$ and $e_1(0)$ can be obtained. Then there is no need to prove the reachability. However, in real applications, the NPC converter will be precharged before the controller starts to work, and the exact $e(0)$ and $e_1(0)$ can not be obtained. In this case, the initial values can be roughly estimated, which can still decrease the distance from the original value of sliding-mode variable to zero, and reduce the convergence time. But this will cause the sliding-mode variables at the beginning close to zero but rather than zero, then, the prove of reachability is necessary.

Next, the way to tune the parameters of the proposed control strategy is shown. For the parameters of ESO, assume the disturbance $d_j = \int_0^t h(s)ds$, then the transfer function can be calculated as (47) based on (24). The unit step response of (47) can be described as (48).

$$G(s) = \frac{\omega_j^2}{(s+\omega_j)^2}, \tag{47}$$

$$Y(s) = \frac{\omega_j^2}{(s+\omega_j)^2} \cdot \frac{1}{s},$$

$$y(t) = 1 - \exp^{-\omega_j t}(1+\omega_j t). \tag{48}$$

Hence, the convergence time of estimation error can be calculated by substituting the maximum value of steady-state estimation error (defined by the operator) into (48).

For power tracking loop, the convergence time t_p of e can be calculated as $t_p = t_{p1} + t_{p2}$, where t_{p1} is the convergence time of Lyapunov function V and t_{p2} is the convergence time of e since the sliding-mode surface σ is reached. Next, the equations of t_{p1} and t_{p2} will be shown.

The derivative of (30) can be rewritten as (49) based on the assumption that sliding-mode surface is reached when the magnitude of σ arrives 10^{-4}.

$$\begin{aligned} \dot{V} &\le -\beta(\varpi - \tilde{d}_M)(|\sigma_p| + |\sigma_q|) \\ &\le -\beta(\varpi - \tilde{d}_M)\left((\sigma_p) + (\sigma_q)\right)^{\frac{1}{2}} \\ &\le -\beta(\varpi - \tilde{d}_M)\sqrt{2V}. \end{aligned} \tag{49}$$

Define $l_1 = \sqrt{2}\beta(\varpi - \tilde{d}_M)$, then (49) can be rewritten as (50), and the convergence time t_{p1} of V can be obtained as (51).

$$\dot{V} \le -l_1\sqrt{V}, \tag{50}$$

$$t_{p1} \le \frac{2}{l_1}V(0)^{\frac{1}{2}}, \tag{51}$$

where $V(0)$ is the initial value of Lyapunov function.

From the derivative of power tracking error e in (31), the dynamic response of e can be obtained as

$$e = e(0)\exp^{(-\frac{x_1}{2L}||v_{\alpha\beta}||^2 k_1 t)}, \tag{52}$$

where $e(0)$ is the initial value of e when the sliding-mode surface σ is reached. Then t_{p2} can be obtained by defining the error band (which is usually 2% or 5%). With above equations, the parameters of power tracking loop can be selected based on the convergence time t_p defined by the operator.

It's the same case for the voltage regulation loop, the convergence time t_v of DC-link voltage can be calculated as $t_v = t_{v1} + t_{v2}$, where t_{v1} is the convergence time of Lyapunov function V_v and t_{v2} is the convergence time of e_1 since the sliding-mode surface σ_v is reached. The equations of t_{v1} and t_{v2} will be shown. The derivative of (43) can be rewritten as (53).

$$\begin{aligned} \dot{V}_v &= -k_N\alpha\frac{C}{2}(\sigma_v)^2 \\ &= -k_N\alpha C\left(V_v - \frac{1}{2}\alpha\tilde{\Theta}^T\tilde{\Theta}\right) \\ &= -l_2V_v + l_3, \end{aligned} \tag{53}$$

where $l_2 = k_N \alpha C$ and $l_3 = \frac{1}{2}\alpha^2 k_N C\tilde{\Theta}^T\tilde{\Theta}$. Define $l_{3M} = \sup_{t>0}(|l_3|)$, the convergence time t_{v1} can be obtained as

$$t_{v1} \leq \frac{\ln(1 - \frac{l_2}{l_{3M}} V_v(0))}{l_2}, \tag{54}$$

where $V_v(0)$ is the initial value of Lyapunov function. The dynamic response of e_1 can be obtained as (55) from (44), and convergence time t_{v2} of regulation error e_1

$$e_1 = e_1(0)\exp^{(-\frac{2}{C}k_v t)}, \tag{55}$$

where $e_1(0)$ is the initial value of e_1 when the sliding-mode surface σ_v is reached. Then t_{v2} can be obtained by defining the error band (which is usually 2% or 5%). With above equations, the parameters of voltage regulation loop can be selected based on the convergence time t_v defined by designer.

Summarizing, the process of parameters selecting can be divided into the following steps.

1. Define the convergence time t_{v1} and t_{v2} (or t_{p1} and t_{p2}).
2. Define the error band of e_1 (or e), then the maximum value of steady-state voltage regulation error e_{1M} (or steady-state maximum power tracking error e_M) can be obtained.
3. Substitute e_{1M} and t_{v2} (or e_M, t_{p2}) into (55) (or (52)), then k_v (or k_1) can be obtained.
4. Substitute t_{v1} (or t_{p1}) into (54) (or (51)), then k_N, α, c and δ (or ϖ based on ω_j obtained from (47) and β) can be obtained.

5. Experimental Results

Several experimental results, of both the proposed ISMC-based DPC strategy and PI-based DPC strategy, are shown in this section. The effectiveness of the proposed control strategy is validated. The prototype of the NPC converter system is shown in Figure 7. The controller and the LS-PWM strategy are implemented in a DSP (TMS320F28377D) control platform. The parameters of the laboratory prototype are shown in Table 2. The PI-based DPC strategy for the NPC converter and the way to select the parameters of PI-based DPC are included in the Appendix A. The way to select the parameters of the proposed control strategy is addressed in Section 4. The control parameters of both control strategies are shown in Table 3. The experimental results can be split-off in dynamic as well as the steady-state performance.

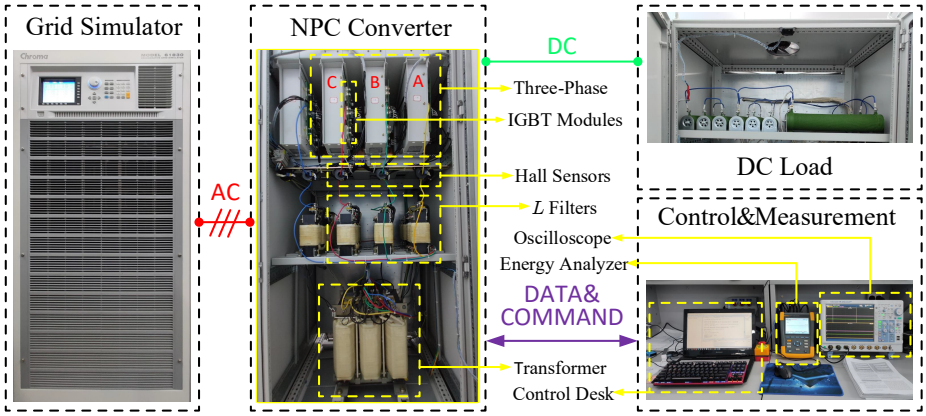

Figure 7. Prototype of NPC converter system.

Table 2. System parameters.

Description	Parameter	Value
Phase inductor	L (mH)	2
DC-link capacitor	C (mF)	6
Load resistance	R_{dc} (Ω)	$0 \rightarrow 150$
Grid frequency	ω (Hz)	50
Sampling frequency	f_s (Hz)	6400
Grid line voltage	v_{abc} (V_{rms})	400
Desired DC-link voltage	x_1^* (V)	750

Table 3. Control parameters.

	PI-Based DPC Strategy	ISMC-Based DPC Strategy
Power tracking loop	$\omega_p = 10,\ \omega_q = 100,$ $k_1 = 9 \cdot 10^{-8},\ \beta = 10^{-5},\ \varpi = 10$	$k_{p1} = 2 \cdot 10^{-8},$ $k_{i1} = 10^{-7}$
Voltage regulation loop	$c = [2,\ 0,\ -2],\ \mu = 100,$ $\alpha = 1.8 \cdot 10^{-9},\ k_v = 0.1,\ k_N = 3.5 \cdot 10^{13}$	$k_{p2} = 0.1,$ $k_{i2} = 2$
Voltage balancing loop	$k_{pb} = 8.66 \cdot 10^{-3},\ k_{ib} = 1.73 \cdot 10^{-5}$	$k_{p3} = 8.66 \cdot 10^{-3},\ k_{i3} = 1.73 \cdot 10^{-5}$

5.1. Dynamic Performance Experiment

To show the disturbance rejection ability of both controllers, a variation of load resistance R_{dc} from no load to 150 Ω is applied. In this section, the most important features are voltage drop and recovery time. The dynamics of DC-link voltage, active power, reactive power of both controllers and the voltages of the two DC-link capacitors are shown in Figure 8.

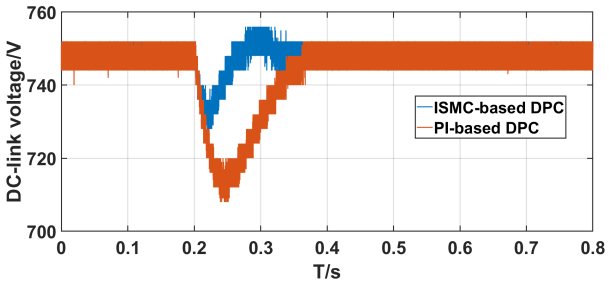

(**a**)

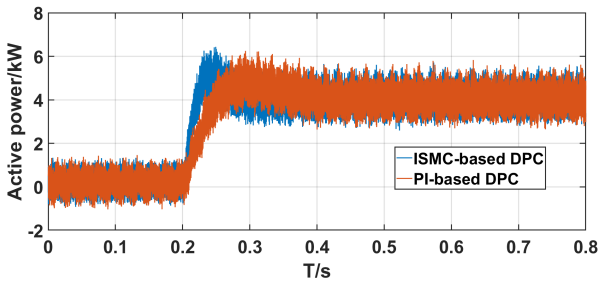

(**b**)

Figure 8. *Cont.*

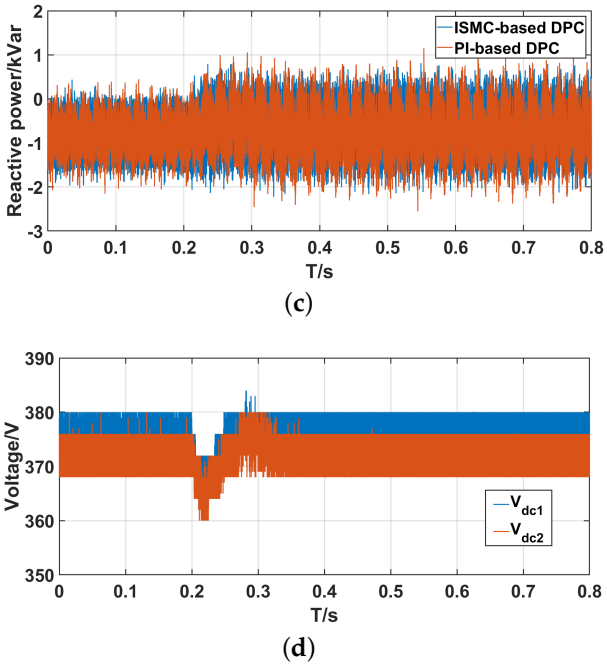

Figure 8. Dynamic reponse of DC-link voltage, active power, reactive power and voltages of two DC-link capacitors. (**a**) DC-link voltage; (**b**) Active power; (**c**) Reactive power; (**d**) Voltages of two capacitors.

Comparing the results of both controllers, it can be seen that both controllers can achieve the three objectives defined in (10)–(12). Both controllers are able to regulate the output voltage x_1 to its reference value x_1^* despite the load variation, and force the active power and reactive power to track their reference values. The objective of voltage balance is also achieved. It has to be noticed that a better system performance is obtained by using the proposed control strategy. The unavoidable voltage drop has been reduced in amplitude from 40 V to 22 V. In the meantime, the recovery time of the proposed control strategy presents a smaller value 0.12 s compared with the 0.16 s of the PI-based DPC. The voltage regulation ability and disturbance rejection ability of the proposed controller have been verified. Due to the same parameters of voltage balancing loops of both controllers, the voltages of the two DC-link capacitors present the same response for both control strategies, hence it only show once. It can be seen that the voltages of the two DC-link capacitors are almost the same despite the load variation, which verifies the effectiveness of voltage balancing loop.

5.2. Steady-State Performance Experiment

In this section, the load resistance is kept at 150 Ω, the inductor currents and their corresponding harmonic spectrum are shown in Figures 9 and 10. It can be seen that the current harmonic spectrum of the proposed strategy is almost the same compared to that obtained by the PI-based DPC strategy, which shows a similar control performance for power tracking loop in steady-state.

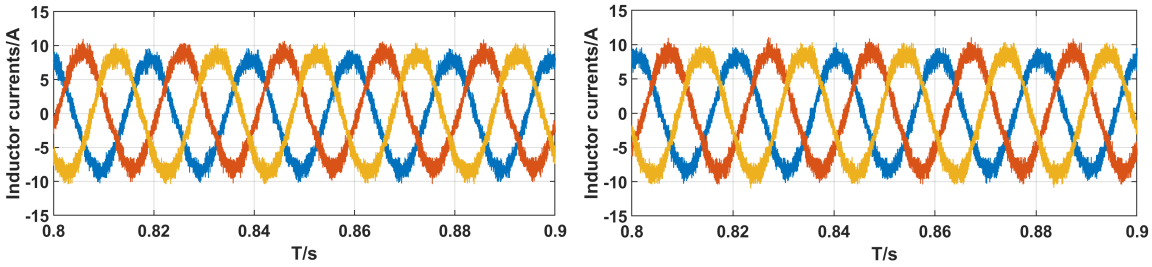

Figure 9. Inductor currents of both controllers. (**a**) PI-based DPC; (**b**) ISMC-based DPC.

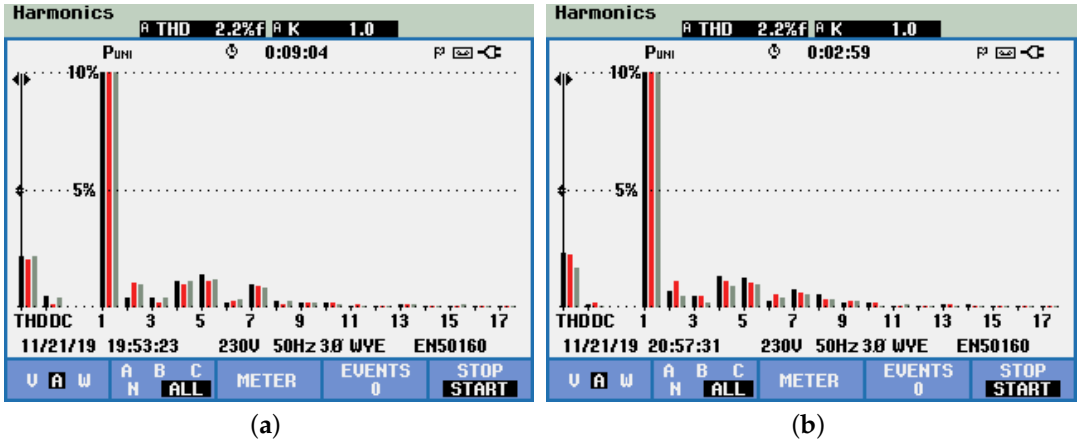

Figure 10. Harmonic spectrum of inductor currents of both controllers. (**a**) PI-based DPC; (**b**) ISMC-based DPC.

6. Conclusions

In this paper, an ISMC-based DPC strategy is proposed for three-level NPC converter which is a very attractive solution in high-power energy conversion system. ESO and RBFNN are used to reduce the impact of parameter uncertainties such as inductors and grid frequency value, and disturbances such as load variation. With the ISMC strategy, the convergence time of the tracking error is reduced. The adaptive law used in the voltage regulation loop reduces the active power reference chattering, which helps to reduce the current THD. The good steady-state and dynamic performance of the proposed control strategy have been evaluated in a three-phase three-level NPC converter. The experimental results indicate that comparing with PI-based DPC strategy, the smaller transient voltage drop and shorter recovery time against load resistance variation can be obtained by the proposed ISMC-based DPC strategy.

Author Contributions: Methodology, H.L.; writing–original draft preparation, H.L.; writing–review and editing, J.I.L. and A.M.; supervision, W.L., J.L., L.G.F. and S.V. All authors have read and agreed to the published version of the manuscript.

Funding: This work was supported in part by the National Natural Science Foundation of China (61525303, 41772377 and 61673130), Top-Notch Young Talents Program of China (Ligang Wu), State grid heilongjiang electric power company limited funded project and the Self-Planned Task of State Key Laboratory of Robotics and System (HIT) (SKLRS201806B).

Conflicts of Interest: The authors declare no conflict of interest.

Abbreviations

The following abbreviations are used in this manuscript:

AFE	active front end
NPC	Neutral-point-clamped
ISMC	Integral sliding-mode control
SMC	Sliding-mode control
ESO	Extended state observer
DPC	Direct power control
RBFNN	Radial basis function neural network
PI	Proportional-integral
LS-PWM	level shifted-pulse width modulation
THD	Total harmonic distortion

Appendix A. PI-Based DPC for NPC Converter

The PI-based DPC strategy presents different control loops. In the power tracking loop, the control law is (A1). In the voltage regulation loop, the control law is (A2). In the voltage balancing loop, the control law is (A3).

$$
\begin{aligned}
u_{\alpha\beta}^{eq} &= \frac{2}{x_1||v_{\alpha\beta}||^2}\left[\left(||v_{\alpha\beta}||^2 + L\omega q\right)v_{\alpha\beta} - L\omega p J v_{\alpha\beta}\right] \\
u_{\alpha\beta} &= u_{\alpha\beta}^{eq} - \mu(e_p)v_{\alpha\beta} - \mu(e_q)Jv_{\alpha\beta} \\
\mu(e_p) &= k_{p1}e_p + k_{i1}\int_0^t e_p ds \\
\mu(e_q) &= k_{p1}e_q + k_{i1}\int_0^t e_q ds, \qquad \text{(A1)} \\
u_v &= k_{p2}e_1 + k_{i2}\int_0^t e_1 ds, \qquad \text{(A2)} \\
u_\gamma &= -k_{p3}x_2 - k_{i3}\int_0^t x_2 ds. \qquad \text{(A3)}
\end{aligned}
$$

Next, the way to select the parameters will be introduced. For the power tracking loop, voltage regulation loop and voltage balancing loop, the open-loop transfer functions can be calculated as (A4)–(A6), respectively.

$$
\begin{aligned}
G_1(s) &= -B\frac{k_{p1}s + k_{i1}}{s^2}, \qquad \text{(A4)} \\
G_2(s) &= \frac{2}{C}\frac{k_{p2}s + k_{i2}}{s^2 + \frac{4}{R_{dc}C}s}, \qquad \text{(A5)} \\
G_3(s) &= \frac{2p^*}{\sqrt{6}Cx_1}\frac{k_{p3}s + k_{i3}}{s^2}. \qquad \text{(A6)}
\end{aligned}
$$

Considering that in the real application, the sampling period results in a delay in the output. Therefore, the transfer functions (A4)–(A6) all multiply $\exp^{(-1.5T_s s)}$, where $T_s = \frac{1}{f_s}$ is the sampling period, and discretize them. The bode diagrams of the functions are shown in Figures A1–A3.

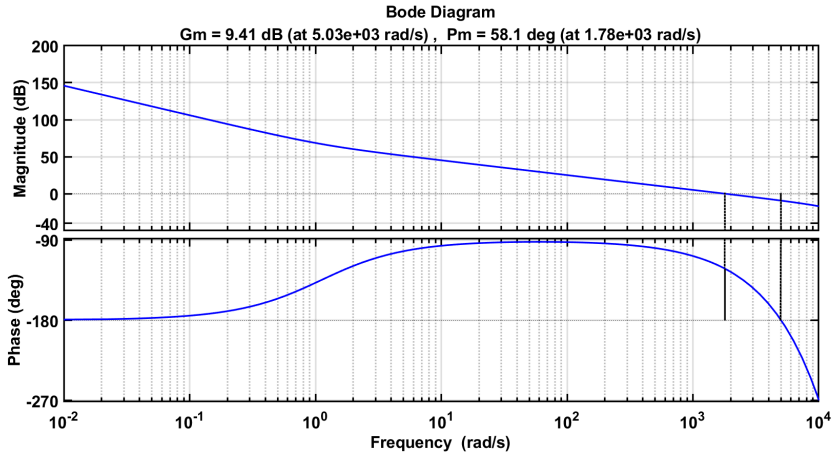

Figure A1. Bode diagram for transfer function of power tracking loop.

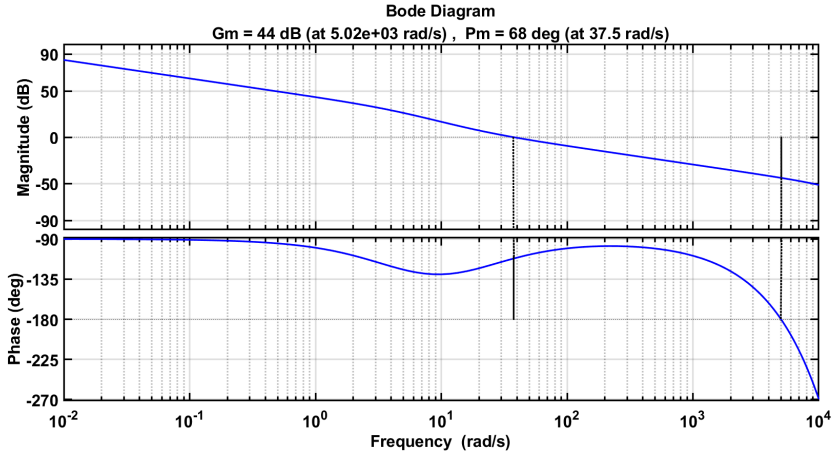

Figure A2. Bode diagram for transfer function of voltage regulation loop.

The gain margins G_m and phase margins P_m are shown at the top of the figures. The open-loop cut-off frequency ω_c is the frequency when G_m is zero, and is shown in the parentheses behind P_m. The system will be stable once G_m and P_m are greater than zero.

For the high-order system and non-typical second-order system, the relationship between the frequency response and time domain response is not as simple as that of the typical second-order system. Through the study of a large number of systems in the control engineering practice, the following equations can be used to calculate the overshoot $\sigma\%$ and settling time t_s [33].

$$\sigma\% = (0.16 + 0.4(M_r - 1)) \times 100\%, \tag{A7}$$

$$t_s = \frac{\pi}{\omega_c}\left(2 + 1.5\,(M_r - 1) + 2.5(M_r - 1)^2\right), \tag{A8}$$

where $M_r = \frac{1}{\sin P_m}$ and $1 \leq M_r \leq 1.8$, which means $34^\circ \leq P_m \leq 90^\circ$.

From the above equations, it can be observed that the overshoot will decrease when phase margin increases, and the settling time will decrease when open-loop cut-off frequency increase. With this way, the parameters can be selected based on the constraints and requirements. In this paper, it can be seen that all the gain margins and phase margins are greater than zero, which verifies the stability of the systems. It can be calculated that for the power tracking loop, the overshoot $\sigma_p\% = 23.12\%$ and settling time $t_{sp} = 4.1\ \ ms$. For the voltage regulation loop, the overshoot $\sigma_v\% = 19.14\%$ and settling time $t_{sv} = 0.18\ \ s$. The fast convergence rate and low overshoot of power tracking loop and voltage regulation loop have been guaranteed. For the voltage balancing loop, considering that there will be no

step in the input x_2^* due to $x_2^* = 0$, the PI parameters only need to guarantee the stability, which means G_m and P_m of voltage balancing loop only need to be greater than zero.

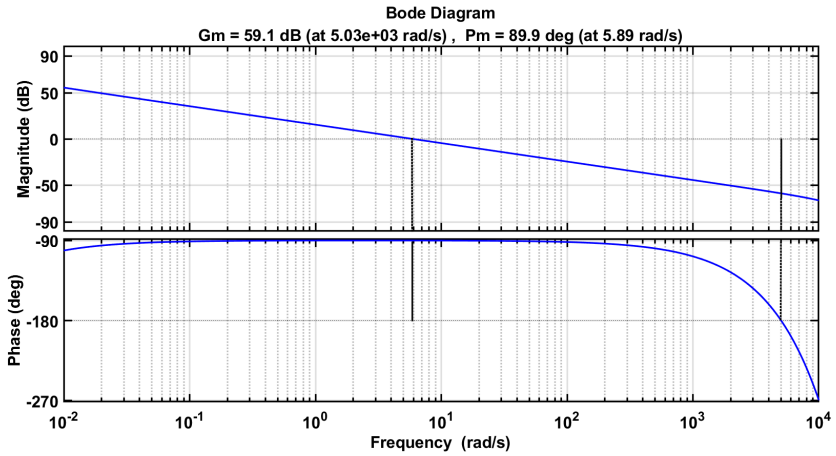

Figure A3. Bode diagram for transfer function of voltage balancing loop.

References

1. Sayed-Ahmed, A.; Seibel, B.; Kerkman, R.J. Active front end motor-drive system operation under power and phase loss. In Proceedings of the 2018 IEEE Applied Power Electronics Conference and Exposition (APEC), San Antonio, TX, USA, 4–8 March 2018; pp. 552–559.
2. Vazquez, S.; Leon, J.I.; Franquelo, L.G.; Rodriguez, J.; Young, H.A.; Marquez, A.; Zanchetta, P. Model predictive control: A review of its applications in power electronics. *IEEE Ind. Electron. Mag.* **2014**, *8*, 16–31. [CrossRef]
3. Vazquez, S.; Marquez, A.; Aguilera, R.; Quevedo, D.; Leon, J.I.; Franquelo, L.G. Predictive optimal switching sequence direct power control for grid-connected power converters. *IEEE Trans. Ind. Electron.* **2015**, *62*, 2010–2020. doi:10.1109/TIE.2014.2351378. [CrossRef]
4. Prakash P.S.; Kalpana, R.; Singh, B.; Bhuvaneswari, G. Design and implementation of sensorless voltage control of front-end rectifier for power quality improvement in telecom system. *IEEE Trans. Ind. Appl.* **2018**, *54*, 2438–2448. [CrossRef]
5. Rodriguez, J.R.; Dixon, J.W.; Espinoza, J.R.; Pontt, J.; Lezana, P. PWM regenerative rectifiers: State of the art. *IEEE Trans. Ind. Electron.* **2005**, *52*, 5–22. [CrossRef]
6. Marzoughi, A.; Burgos, R.; Boroyevich, D. Optimum design guidelines for the modular multilevel converter in active front-end applications: Considerations for passive component reduction. *IEEE Power Electron. Mag.* **2018**, *5*, 56–65. [CrossRef]
7. Leon, J.I.; Vazquez, S.; Franquelo, L.G. Multilevel converters: Control and modulation techniques for their operation and industrial applications. *Proc. IEEE* **2017**, *105*, 2066–2081. [CrossRef]
8. Marzoughi, A.; Burgos, R.; Boroyevich, D.; Xue, Y. Investigation and design of modular multilevel converter in AFE mode with minimized passive elements. In Proceedings of the 2015 IEEE Energy Conversion Congress and Exposition (ECCE), Montreal, QC, Canada, 20–24 September 2015; pp. 6770–6776.
9. Leon, J.I.; Kouro, S.; Franquelo, L.G.; Rodriguez, J.; Wu, B. The essential role and the continuous evolution of modulation techniques for voltage-source inverters in the past, present, and future power electronics. *IEEE Trans. Ind. Electron.* **2016**, *63*, 2688–2701. [CrossRef]
10. Portillo, R.; Vazquez, S.; Leon, J.I.; Prats, M.M.; Franquelo, L.G. Model based adaptive direct power control for three-Level NPC converters. *IEEE Trans. Ind. Inform.* **2013**, *9*, 1148–1157. [CrossRef]
11. Akagi, H.; Kanazawa, Y.; Nabae, A. Instantaneous reactive power compensators comprising switching devices without energy storage components. *IEEE Trans. Ind. Appl.* **1984**, *IA-20*, 625–630. [CrossRef]
12. Malinowski, M.; Jasinski, M.; Kazmierkowski, M.P. Simple direct power control of three-phase PWM rectifier using space-vector modulation (DPC-SVM). *IEEE Trans. Ind. Electron.* **2004**, *51*, 447–454. [CrossRef]

13. Aurtenechea, S.; Rodriguez, M.A.; Oyarbide, E.; Torrealday, J.R. Predictive direct power control—A new control strategy for DC/AC Converters. In Proceedings of the IECON 2006—32nd Annual Conference on IEEE Industrial Electronics, Paris, France, 6–10 November 2006; pp. 1661–1666.
14. Raviraj, V.S.C.; Sen, P.C. Comparative study of proportional-integral, sliding mode, and fuzzy logic controllers for power converters. *IEEE Trans. Ind. Appl.* **1997**, *33*, 518–524. [CrossRef]
15. Kazmierkowski, M.P.; Malesani, L. Current control techniques for three-phase voltage-source PWM converters: A survey. *IEEE Trans. Ind. Electron.* **1998**, *45*, 691–703. [CrossRef]
16. Ríos, H.; Kamal, S.; Fridman, L.M.; Zolghadri, A. Fault tolerant control allocation via continuous integral sliding-modes: A HOSM-observer approach. *Automatica* **2015**, *51*, 318–325. [CrossRef]
17. Subramaniam, R.; Joo, Y.H. Passivity-based fuzzy ISMC for wind energy conversion systems with PMSG. *IEEE Trans. Syst. Man Cybern. Syst.* **2019**, 1–10. [CrossRef]
18. Pan, Y.; Yang, C.; Pan, L.; Yu, H. Integral sliding mode control: Performance, modification, and improvement. *IEEE Trans. Ind. Inform.* **2018**, *14*, 3087–3096. [CrossRef]
19. Hamayun, M.; Edwards, C.; Alwi, H. *Fault Tolerant Control Schemes Using Integral Sliding Modes*; Springer: Berlin/Heidelberg, Germany, 2016.
20. Sun, G.; Wu, L.; Kuang, Z.; Ma, Z.; Liu, J. Practical tracking control of linear motor via fractional-order sliding mode. *Automatica* **2018**, *94*, 221–235. [CrossRef]
21. Shtessel, Y.; Taleb, M.; Plestan, F. A novel adaptive-gain supertwisting sliding mode controller: Methodology and application. *Automatica* **2012**, *48*, 759–769. [CrossRef]
22. Rezaie, B.; Ghasemi, H. Terminal sliding mode controller tuned using evolutionary algorithms for finite-time robust tracking control in a class of nonholonomic systems. *Inf. Technol. Control.* **2018**, *47*, 26–44. [CrossRef]
23. Liu, J.; Gao, Y.; Su, X.; Wack, M.; Wu, L. Disturbance-observer-based control for air management of PEM fuel cell systems via sliding mode technique. *IEEE Trans. Control. Syst. Technol.* **2018**, *27*, 1129–1138. [CrossRef]
24. An, H.; Liu, J.; Wang, C.; Wu, L. Disturbance observer-based antiwindup control for air-breathing hypersonic vehicles. *IEEE Trans. Ind. Electron.* **2016**, *63*, 3038–3049. [CrossRef]
25. Godbole, A.A.; Kolhe, J.P.; Talole, S.E. Performance analysis of generalized extended state observer in tackling sinusoidal Disturbances. *IEEE Trans. Control. Syst. Technol.* **2013**, *21*, 2212–2223. [CrossRef]
26. Chen, W.; Yang, J.; Guo, L.; Li, S. Disturbance-observer-based control and related methods—An overview. *IEEE Trans. Ind. Electron.* **2016**, *63*, 1083–1095. [CrossRef]
27. Jiang, T.; Huang, C.; Guo, L. Control of uncertain nonlinear systems based on observers and estimators. *Automatica* **2015**, *59*, 35–47. [CrossRef]
28. Liu, N.; Fei, J. Adaptive fractional sliding mode control of active power filter based on dual RBF neural networks. *IEEE Access* **2017**, *5*, 27590–27598. [CrossRef]
29. Simone, G.; Morabito, F.C. RBFNN-based hole identification system in conducting plates. *IEEE Trans. Neural Networks* **2001**, *12*, 1445–1454. [CrossRef]
30. Yin, Y.; Liu, J.; Sánchez, J.A.; Wu, L.; Vazquez, S.; Leon, J.I.; Franquelo, L.G. Observer-based adaptive sliding mode control of NPC converters: An RBF neural network Approach. *IEEE Trans. Power Electron.* **2019**, *34*, 3831–3841. [CrossRef]
31. Elanayar V.T., S.; Shin, Y.C. Radial basis function neural network for approximation and estimation of nonlinear stochastic dynamic systems. *IEEE Trans. Neural Networks* **1994**, *5*, 594–603. [CrossRef]
32. Han, J. From PID to active disturbance rejection control. *IEEE Trans. Ind. Electron.* **2009**, *56*, 900–906. [CrossRef]
33. Franklin, G.F.; Powell, J.D.; Emami-Naeini, A. *Feedback Control of Dynamic Systems*; Prentice Hall Press: Bergen County, NJ, USA, 2014.